Antenna-Enhanced Photocurrent Microscopy on Single-Walled Carbon Nanotubes at 30 nm Resolution

Nina Rauhut,[†] Michael Engel,[‡,⊥] Mathias Steiner,[§] Ralph Krupke,[‡,⊥,¶] Phaedon Avouris,[§] and Achim Hartschuh[†,*]

[†]Department Chemie and CeNS, Ludwig-Maximilians-Universität, 81377 Munich, Germany, [‡]Institute of Nanotechnology, Karlsruhe Institute of Technology, 76021 Karlsruhe, Germany, [§]IBM Thomas J. Watson Research Center, Yorktown Heights, New York 10598, United States , [⊥]DFG Center for Functional Nanostructures (CFN), 76031 Karlsruhe, Germany, and [¶]Institut für Materialwissenschaft, Technische Universität Darmstadt, 64287 Darmstadt, Germany

ABSTRACT We present the first photocurrent measurements along single carbon nanotube (CNT) devices with 30 nm resolution. Our technique is based on tip-enhanced near-field optical microscopy, exploiting the plasmonically enhanced absorption controlled by an optical nanoantenna. This allows for imaging of the zero-bias photocurrent caused by charge separation in local built-in electric fields at the contacts and close to charged particles that cannot be resolved using confocal microscopy. Simultaneously recorded Raman scattering images reveal the structural properties and the defect densities of the CNTs. Antenna-enhanced scanning photocurrent microscopy extends the available set of scanning-probe techniques by combining high-resolution photovoltaic and optical probing and could become a valuable tool for the characterization of nanoelectronic devices.

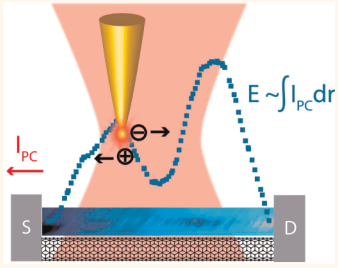

KEYWORDS: single-walled carbon nanotubes · optical antennas · tip-enhanced near-field optical microscopy · scanning photocurrent microscopy · nanoscale devices

Scanning photocurrent microscopy (SPCM) is a powerful tool to investigate the properties of nanoelectronic devices such as carbon nanotube- (CNT),[1−3] graphene-[4,5] or inorganic nanowire-[6,7]based field-effect transistors. In this technique a focused laser beam is raster scanned across a device and the generated photocurrent is recorded at the same time. SPCM provides valuable information on any source of built-in electric fields including internal pn-junctions,[8] local defects[9] and nanostructure−metal interfaces.[1−3,10] The latter are part of virtually all nanoscale devices and govern their overall performance.[11−13] At the metal contacts the current signal at zero bias is known to have at least two contributions. One results from the photovoltaic effect, that is, the separation of the photoexcited charge carriers caused by local built-in electric fields. These fields exist at the contact regions due to the formation of energy barriers and could also occur along the nanostructure caused by sample heterogeneities or external perturbations. In the case of CNT FETs consisting of a semiconducting channel, the width and height of the Schottky barriers formed at the contacts determine its switching action, since they control the charge carrier injection into the CNT channel.[1] For metallic CNTs photocurrent signals at the contacts have also been observed and attributed to the formation of energy barriers similar to the case of semiconducting CNTs.[10] Besides the photovoltaic contribution, there is evidence of an additional contribution to the zero bias current signal which stems from the illumination of the electrodes near the contact region.[14−16] This contribution is due to laser heating of one of the electrodes and can be thermoelectric in origin or caused by thermo-assisted tunneling of charge carriers through the energy barrier.

Up to now, nearly all SPCM measurements reported so far have been restricted to a spatial resolution of few hundred nanometers due to the diffraction limited size of the laser focus, making it impossible to optically characterize a device on the nanoscale. Therefore, the photothermal processes at the electrodes and the photovoltaic effect mentioned above could not be separately imaged in the past, since illumination of the band bending region at the contacts goes hand in hand with illumination of the electrodes due to the lack of sufficient spatial resolution. In addition, photovoltaic contributions originating from subdiffraction potential variations along the CNT could not be detected due to spatial averaging.

In this manuscript we present a high-resolution scanning probe technique that merges the fields of photovoltaics and

* Address correspondence to achim.hartschuh@cup.uni-muenchen.de.

Received for review May 4, 2012 and accepted May 27, 2012.

Published online May 28, 2012
10.1021/nn301979c

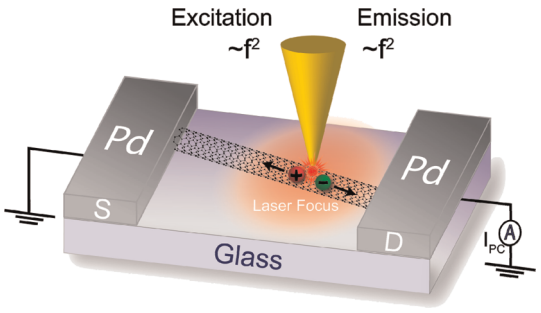

Figure 1. Schematic of antenna-enhanced photocurrent microscopy. The optical antenna locally increases both excitation and emission rates each scaling with the square of the field enhancement factor *f*.[22,23] In near-field microscopy this is optically detected for example *via* tip-enhanced Raman scattering scaling with approximately f^4.[24] In antenna-enhanced photocurrent microscopy the increased excitation rate leads to a stronger photocurrent $\sim f^2$ as demonstrated here for an electrically contacted carbon nanotube.

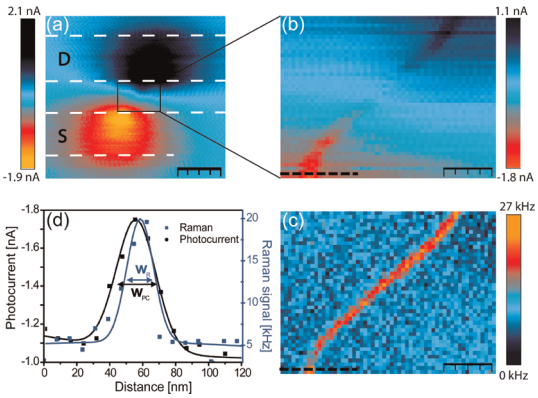

Figure 2. Antenna-enhanced imaging of a single CNT. (a) Confocal photocurrent image of device A. The positions of source (S) and drain (D) electrodes are indicated by dashed white lines. The scalebar indicates 1 μm. (b and c) Antenna-enhanced photocurrent and Raman images obtained by scanning the black rectangular region in panel a. The Raman image represents the G-band intensity measured as photon count rate. The rather uniform Raman signal intensity indicates an almost constant antenna enhancement. The scalebar is 100 nm. (d) Cross sections taken along the dashed black lines in panels b and c together with their Gaussian fits. The spatial resolution of the photocurrent image taken as the full width at half-maximum w_{PC} is about 28 nm. The value obtained from the Raman signal is w_R = 19 nm, about a factor of $1/\sqrt{2}$ smaller.

plasmonics. It exploits the strong electromagnetic field enhancement in the vicinity of an illuminated metallic nanoparticle to locally increase the absorption and hence charge carrier generation in nearby photoactive materials.[17,18] We experimentally demonstrate a new realization of this concept using a sharp gold tip that acts as a nanoantenna converting free-propagating radiation into localized energy and vice versa[19,20] (see Figure 1). We apply this technique to CNT-based devices and use it to simultaneously probe potential modulations of the electronic bands and the Raman scattering signature with sub 30 nm resolution. Besides achieving superior resolution as compared to previous confocal and near-field optical photocurrent studies,[4,21] the present technique is also shown to provide improved detection sensitivity for both photovoltaic and optical probing.

RESULTS AND DISCUSSION

Figure 2a displays a confocal photocurrent image of a contacted carbon nanotube with an electrode separation of about 500 nm (device A) depicting two almost symmetric signals of opposite signs occurring at the source (S) and drain (D) electrode, the typical features of a diffraction-limited SPCM image.[1−3,10,25] The frequency of the radial breathing mode (RBM) of 190 cm^{-1} obtained by Raman spectroscopy (see Supporting Information, Figure 1) and the resonance condition at the laser wavelength of 632.8 nm indicate that the nanotube is metallic.[26]

Antenna-enhanced photocurrent and Raman images of device A, presented in Figure 2 panels b and c, respectively, are obtained by scanning the sample with respect to a metal tip centered in the laser focus in close proximity. The photocurrent image in Figure 2b shows two narrow subdiffraction contributions of opposite sign extending from the electrode regions following the Raman signature of the carbon nanotube in Figure 2c. In scanning probe microscopy the width of the signal can be taken as the spatial resolution, which in general scales with the diameter of the probe. The width of the cross section w_{pc} taken along the black dashed line in the photocurrent image in Figure 2b shown together with its corresponding Gaussian fit function in Figure 2d demonstrates a spatial resolution of about 28 nm. We thus conclude that the enhanced photocurrent signal originates from a 28 nm long nanotube section located underneath the scanning tip. The width of the simultaneously recorded Raman signal w_R at the same position is about 19 nm (see Figure 2d). The ratio between the line width of photocurrent and Raman signal of $w_{PC}/w_R = 28/19 = 1.47$ is approximately equal to $\sqrt{2}$ and is nearly constant along the whole CNT (see Supporting Information, Figure 2). This ratio is expected from the model depicted in Figure 1 considering the enhancement mechanisms of optically and electrically detected signals. The antenna-enhanced fields cause increased excitation and, due to reciprocity, emission rates. The field enhancement factor f is usually defined as the ratio between the local electric field at the tip and the incident field $f = E_{tip}/E_0$. The enhancement of the excitation rate is thus given by $k_{ex,tip}/k_{ex,0} = f^2$. In the case of Raman scattering in CNTs where the excitation wavelength is close to the emission wavelength of the G-band similar enhancement factors result for excitation and emission. The intensity of optically detected Raman scattering I_R hence scales with f^4. A factor of $\sqrt{2}$ for the ratio of the linewidths of the Gaussian cross sections suggests that $I_R \sim (I_{PC})^2$, which implies that the enhanced photocurrent signal scales with f^2. This is consistent with the fact that for the electrically detected

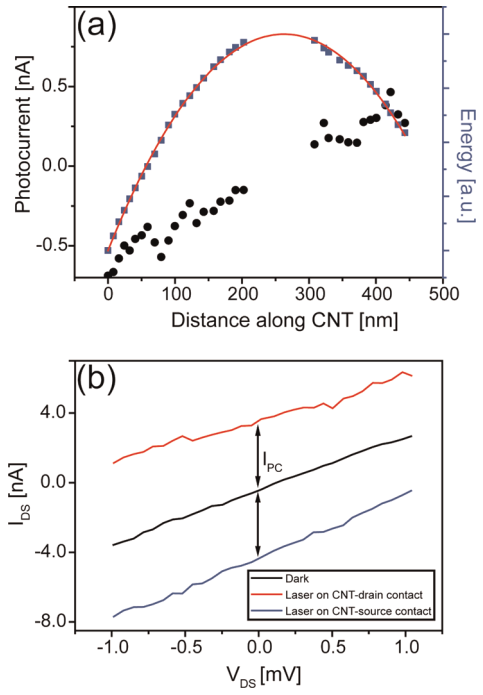

Figure 3. Band bending. (a) Antenna-enhanced photocurrent signal along the CNT of device A (black round symbols). The missing data points in the middle correspond to the region where the enhanced signal was too weak to perform a Gaussian fit. The photocurrent signal integrated in space along the CNT reconstructs the band energy profile (blue square symbols) fitted by a sum of two exponential decay curves with opposite sign (red curve) resulting in a common decay length of $l = 517 \pm 210$ nm. The large uncertainty is due to the superposition of symmetric band bending contributions from the two contacts with opposite sign that cancel in the middle of the CNT and does not reflect signal noise. (b) Source−drain $I-V$ curves recorded under confocal illumination of the nanotube at either source or drain electrode. The curves experience either a positive or negative offset I_{PC} indicating the direction of electron flow at the respective electrodes.

photocurrent signal the enhancement only affects the excitation rate.

By performing Gaussian fits for each line in Figure 2b the antenna-enhanced signal can be extracted from the background resulting from confocal far-field excitation of the CNT and the electrode region. Its amplitude along the nanotube is plotted in Figure 3a. Since the enhancement takes place within a nanotube section of about 30 nm at the position of the antenna at distances of up to few 100 nm away from the electrodes, we conclude that the enhanced photocurrent signal cannot be due to laser-illumination of the electrode, but results from locally enhanced optical excitation of the CNT. Separation of the photoexcited charge carriers at zero bias requires a local built-in electric field that stems from band bending at the metal contacts extending into the CNT. Its decay length l is quantified in the following. For 1D nanostructures linear scaling between the photocurrent I_{PC} and the electric field expressed as the band gradient corresponding to $I_{PC} \sim -dE/dr$ has been reported, where r denotes the position along the structure and E is the energy of the electronic band.[3,9] Integrating the photocurrent signal recorded along the CNT in Figure 2b, one obtains the band energy profile. The band profile can be well described by the sum of two exponential decay curves with equal decay length l and amplitude shown as a red curve in Figure 3a (see Supporting Information, eq 1 for the fit function). The common decay length of the two single exponentials is $l = 517$ nm ± 210 nm. Our results are in agreement with theoretical predictions, stating that the band energy of a CNT decays exponentially with the distance from the contacts due to its small geometry.[27]

From the enhanced Raman and photocurrent signals we estimate the photocarrier quantum efficiency defined as the ratio between the number of created carriers and absorbed photons to be on the order of 10^{-3} close to the contacts (for details see Supporting Information, Note 1). We note that local laser heating along the CNT followed by heat transport could in principle lead to an asymmetric temperature increase at the electrodes resulting in an indirect photothermal contribution to the detected current. This contribution from a nanoscale CNT section is expected to be far smaller than what is observed upon direct confocal illumination of one of the macroscopic electrodes (see Figure 2a). However, our experimental data for confocal and antenna-enhanced photocurrent signals are on the same order of magnitude, which indicates that local laser heating along the CNT is not the dominating process.

Figure 3a indicates a downward bending of the band at the contacts. This is confirmed by $I-V$ curves recorded illuminating the CNT at either source or drain contact (Figure 3b). From the dark curve it becomes evident that a positive current corresponds to an electron flow from source to drain. Illuminating the drain contact offsets the $I-V$ curve by a positive photocurrent I_{PC} implying that additional electrons flow onto the drain electrode. From this we conclude that a positive photocurrent corresponds to a downward band bending. To summarize our findings for device A, antenna-enhanced photocurrent microscopy allowed us to image the photovoltaic contribution separately from the electrode contribution and to resolve the spatial extension of the band bending at the metal contacts that can be described by an exponential decay.

A second metallic device B with longer channel length ($\sim 1\ \mu$m) was investigated to study band energy fluctuations along a single nanotube. As for device A, the metallic character of the CNT was deduced from the Raman spectrum (see Supporting Information, Figure 1). Figure 4 panels b and c show the simultaneously recorded antenna-enhanced photocurrent and Raman G-band images. In contrast to device A, device B exhibits an additional change of sign of the

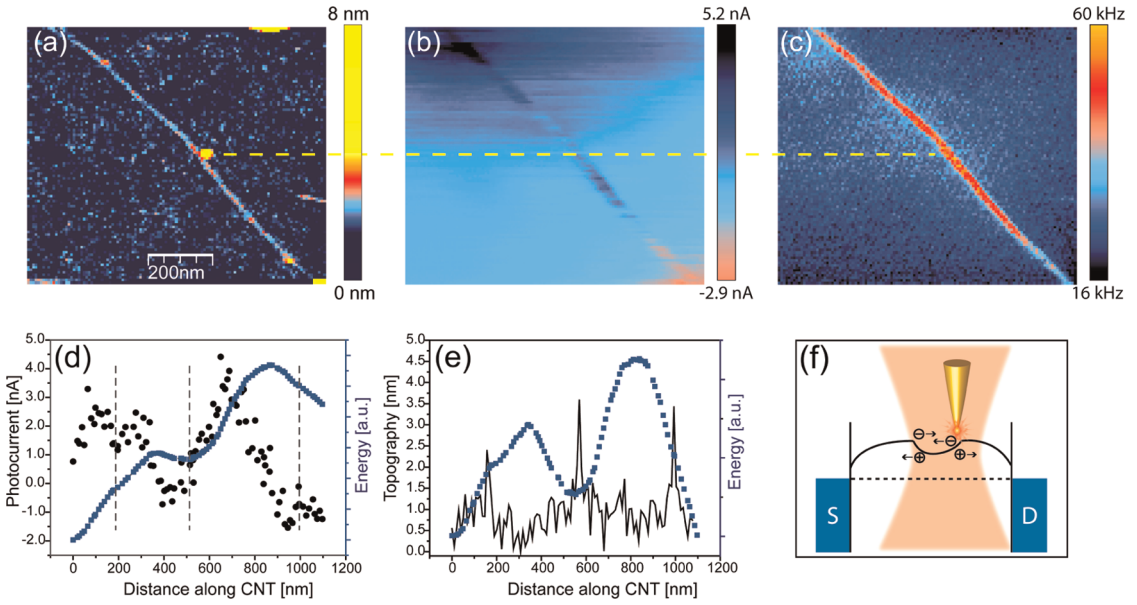

Figure 4. Antenna-enhanced imaging of photocurrent fluctuations along a single CNT (device B). (a) Topography image. The drain and source electrodes appear at the top and at the bottom of the image. (b and c) Antenna-enhanced photocurrent and Raman G-band image. The scalebar is the same as in panel a. The dashed yellow line marks the position of the central particle. (d) Amplitude of fitted antenna-enhanced photocurrent signal along the CNT (black round symbols). The integrated photocurrent signal (blue square symbols) reconstructs the shape of the band potential. (e) The integrated photocurrent signal from panel d after a slope subtraction (blue symbols). The local minimum and kinks in the band energy profile seen in panels d and e coincide with the locations of particles seen as peaks in the topography data (black curve in panel e and marked in panel d by dashed vertical lines). (f) Schematic band diagram. The local minimum cannot be resolved with a diffraction limited laser spot due to spatial averaging of photocurrent signals with opposite signs.

photocurrent occurring in the middle of the device, approximately at the position of the dashed horizontal yellow line in Figures 4a–c. This change of sign indicates that the photocurrent is not caused by an asymmetric temperature increase at the electrodes after local laser heating along the CNT and supports its assignment to charge separation by local built-in electric fields. The effect of direct confocal laser heating of the electrodes exists and is shown for device B in the Supporting Information, Figure 3.

Integrating the photocurrent signal along the length of the nanotube reconstructs the band energy profile as discussed above (Figure 4d). The band features a linear offset, which we attribute to charging of the substrate during the scanning process.[9] Figure 4e shows the result after slope subtraction together with the topography profile along the CNT. The local minimum in the electronic band of the CNT at 570 nm coincides exactly with the position of a particle seen in the topography data in Figure 4a,e. We thus attribute the additional photocurrent signal to the presence of charges associated with this particle. The derived band energy profile therefore reflects a superposition of the contributions from the contacts and the particle, making it unfeasible to quantify the decay length of the band bending at the contacts as it was done for device A. However, we note that for both devices the decay happens on the same length scale of few hundred nanometers. Remarkably, the photocurrent fluctuations cannot be detected in the confocal image due

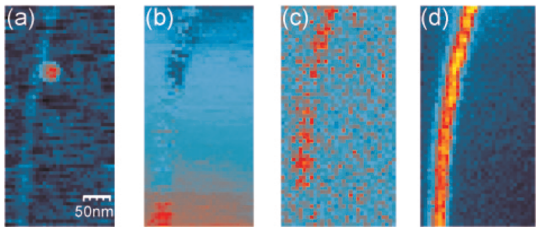

Figure 5. High-resolution spectroscopic imaging of the central region of device B: (a) topography, (b) photocurrent, (c) Raman D-band intensity, (d) Raman G-band intensity taken along device B containing the particle seen in the center of Figure 4a. A varying D-band signal strength can be observed along the CNT, but without showing any correlation with the photocurrent signal. The scalebar indicating 50 nm is the same in every image. In this measurement, complete Raman spectra were taken at each image pixel. The Raman D- and G-band intensities were derived by integrating the respective spectral contribution.

to spatial averaging (see Figure 4f and Supporting Information, Figure 3). Upon closer inspection of the near-field data, two less pronounced photocurrent signatures at 150 and 1000 nm can also be correlated with particles occurring in topography (compare Figure 4 panels d and e). On the basis of this spatial correlation we believe that in the present case the observed potential modulations are caused by charged particles rather than structural defects within the CNT reported before.[9] Structural defects in CNTs can be studied by Raman spectroscopy leading to characteristic D-band scattering.[26,28,29] We support our interpretation by recording simultaneous high-resolution

Raman spectroscopic and photocurrent images focusing on the region around the central particle. These images (see Figure 5) show a varying D-band intensity along the CNT indicating the presence of structural defects, but no correlated increase of the photocurrent signal as observed in ref 9.

CONCLUSIONS

We presented antenna-enhanced scanning photocurrent microscopy that enables the simultaneous recording of optical and photocurrent signals with nanoscale spatial resolution and improved detection sensitivity. We showed that the enhanced photocurrent signal is due to locally increased absorption by comparing it to the simultaneously obtained Raman signal. The technique was used to study the direction and decay length of the band bending at the contacts of metallic CNT devices and to probe local variations in the electronic structure along a single CNT that cannot be detected by confocal microscopy. Our results underline the wide applicability of the optical antenna concept in nanophotonics merging the fields of plasmonics and photovoltaics.

METHODS

The experimental setup combines a tip-enhanced near-field optical microscope (TENOM) with a SPCM operating at room temperature in ambient conditions. The TENOM consists of an inverted confocal microscope (60×; NA 1.49) and a focus-centered sharp gold tip which is hold at about 5 nm above the sample surface with a sensitive tuning-fork shear-force feedback. The complete setup is shown in Supporting Information, Figure 4. The gold tips are produced by electrochemical etching resulting in a tip diameter of about 30 nm. A He−Ne laser emitting at 632.8 nm (power ∼1 mW) was focused to a diffraction-limited spot of ∼300 nm diameter. Radial polarization of the beam leads to an efficient field enhancement at the gold tip.[24] Sample images are acquired by raster scanning the sample with respect to the fixed tip and focus position while recording topography, Raman scattering, and photocurrent signals at each image pixel. The Raman G-band intensity is detected by an APD after spectral selection using a narrow band-pass filter centered at 703 nm. Alternatively, full Raman spectra are taken at each image pixel. The intensity of different Raman bands is then obtained by integrating the signal over the respective energy range. The zero-bias photocurrent is first amplified by a current preamplifier followed by lock-in detection. The signal modulation is accomplished with a mechanical chopper in the excitation beam path operating at 870 Hz. In antenna-enhanced scanning photocurrent microscopy the metal tip is not in contact with the sample and not used as the top electrode as it is done in photoconductive AFM[30,31] or scanning gate microscopy.[32] The antenna is floating and electrostatic charging is not observed during the measurement, as expected for a massive, that is, 1 mm long, metal wire. Its only function for the photocurrent measurements is to provide a nanoscale light source inducing locally enhanced photocurrents that are detected as described above. The devices consist of CVD grown carbon nanotubes dispersed in aqueous suspension by sodium cholate and deposited on a thin microscope glass substrate by spin-coating. The nanotubes were contacted by two electrodes consisting of 0.5 nm titanium/30 nm palladium fabricated *via* electron beam lithography.

Conflict of Interest: The authors declare no competing financial interest.

Acknowledgment. We thank P. Altpeter and N. Saxena for support with the sample preparation, M. Handloser for fruitful discussions, and the ERC (starting Grant NEWNANOSPEC) and the German Science Foundation (DFG) through the Nanosystems Initiative Munich (NIM) for funding.

Supporting Information Available: Detailed information on the experimental setup (supporting Figure 1); Raman spectra of the investigated CNTs (supporting Figure 2) that reveal their metallic character; ratio between photocurrent and Raman linewidths determined along device A (supporting Figure 3); contribution of the electrode effect to the photocurrent (supporting Figure 4); details on the estimation of the quantum efficiency; details on the fit function used to fit the band energy profile shown in Figure 3b. This material is available free of charge *via* the Internet at http://pubs.acs.org.

REFERENCES AND NOTES

1. Freitag, M.; Tsang, J. C.; Bol, A.; Yuan, D.; Liu, J.; Avouris, Ph. Imaging of the Schottky Barriers and Charge Depletion in Carbon Nanotube Transistors. *Nano Lett.* **2007**, *7*, 2037–2042.
2. Balasubramanian, K.; Fan, Y.; Burghard, M.; Kern, K.; Friedrich, M.; Wannek, U.; Mews, A. Photoelectronic Transport Imaging of Individual Semiconducting Carbon Nanotubes. *Appl. Phys. Lett.* **2004**, *84*, 2400–2402.
3. Lee, E. J. H.; Balasubramanian, K.; Dorfmüller, J.; Vogelgesang, R.; Fu, N.; Mews, A.; Burghard, M.; Kern, K. Electronic-Band-Structure Mapping of Nanotube Transistors by Scanning Photocurrent Microscopy. *Small* **2007**, *3*, 2038–2042.
4. Xia, F.; Mueller, T.; Golizadeh-Mojarad, R.; Freitag, M.; Lin, Y.; Tsang, J.; Perebeinos, V.; Avouris, Ph. Photocurrent Imaging and Efficient Photon Detection in a Graphene Transistor. *Nano Lett.* **2009**, *9*, 1039–1044.
5. Mueller, T.; Xia, F.; Freitag, M.; Tsang, J.; Avouris, Ph. Role of Contacts in Graphene Transistors: A Scanning Photocurrent Study. *Phys. Rev. B* **2009**, *79*, 245430.
6. Ahn, Y.; Dunning, J.; Park, J. Scanning Photocurrent Imaging and Electronic Band Studies in Silicon Nanowire Field Effect Transistors. *Nano Lett.* **2005**, *5*, 1367–1370.
7. Allen, J. E.; Hemesatz, E. R.; Lauhon, L. J. Scanning Photocurrent Microscopy Analysis of Si Nanowire Field-Effect Transistors Fabricated by Surface Etching of the Channel. *Nano Lett.* **2009**, *9*, 1903–1908.
8. Ahn, Y. H.; Tsen, A. W.; Kim., B.; Park, Y. W.; Park, J. Photocurrent Imaging of p-n Junctions in Ambipolar Carbon Nanotube Transistors. *Nano Lett.* **2007**, *7*, 3320–3323.
9. Freitag, M.; Tsang, J. C.; Bol, A.; Avouris, Ph.; Yuan, D.; Liu, J. Scanning Photovoltage Microscopy of Potential Modulations in Carbon Nanotubes. *Appl. Phys. Lett.* **2007**, *91*, 031101.
10. Balasubramanian, K.; Burghard, M.; Kern, K.; Scolari, M.; Mews, A. Photocurrent Imaging of Charge Transport Barriers in Carbon Nanotube Devices. *Nano Lett.* **2005**, *5*, 507–510.
11. Chen, Z.; Appenzeller, J.; Knoch, J.; Lin, Y.; Avouris, Ph. The Role of Metal−Nanotube Contact in the Performance of Carbon Nanotube Field-Effect Transistors. *Nano Lett.* **2005**, *5*, 1497–1502.
12. Cummings, A. W.; Léonard, F. Enhanced Performance of Short-Channel Carbon Nanotube Field-Effect Transistors Due to Gate-Modulated Electrical Contacts. *ACS Nano* **2012**, *6*, 4494–4499.
13. Avouris, Ph.; Chen, Z.; Perebeinos, V. Carbon-Based Electronics. *Nat. Nanotechnol.* **2007**, *2*, 605–615.
14. Xu, X.; Gabor, M. N.; Alden, J. S.; van der Zande, A. M.; McEuen, P. L. Photothermoelectric Effect at a Graphene Interface Junction. *Nano Lett.* **2010**, *10*, 562–566.

15. St-Antoine, B. C.; Ménard, D.; Martel, R. Position Sensitive Photothermoelectric Effect in Suspended Single-Walled Carbon Nanotube Films. *Nano Lett.* **2009**, *9*, 3503–3508.
16. Freitag, M.; Low, T.; Xia, F.; Avouris, Ph. Photoconductivity of Biased Graphene. arXiv:1202.5342v1 [cond-mat.mes-hall] **2012**.
17. Atwater, H. A.; Polman, A. Plasmonics for Improved Photovoltaic Devices. *Nat. Mater.* **2010**, *9*, 205–213.
18. Schuller, J. A.; Barnard, E. S.; Cai, W.; Jun, Y. C.; White, J. S.; Brongersma, M. L. Plasmonics for Extreme Light Concentration and Manipulation. *Nat. Mater.* **2010**, *9*, 193–204.
19. Bharadwaj, P.; Deutsch, B.; Novotny, L. Optical Antennas. *Adv. Opt. Photonics* **2009**, *1*, 438–483.
20. Novotny, L.; van Hulst, N. Antennas for Light. *Nat. Photonics* **2011**, *5*, 83–90.
21. Gu, Y.; Kwak, E. S.; Lensch, J. L.; Allen, J. E.; Odom, T. W.; Lauhon, L. J. Near-Field Scanning Photocurrent Microscopy of a Nanowire Photodetector. *Appl. Phys. Lett.* **2005**, *87*, 043111.
22. Taminiau, T. H.; Stefani, F. D.; Segerink, F. B.; van Hulst, N. F. Optical Antennas Direct Single-Molecule Emission. *Nat. Photonics* **2008**, *2*, 234–237.
23. Böhmler, M.; Hartmann, N.; Georgi, C.; Hennrich, F.; Green, A. A.; Hersam, M. C.; Hartschuh, A. Enhancing and Redirecting Carbon Nanotube Photoluminescence by an Optical Antenna. *Opt. Express* **2010**, *18*, 16443–16451.
24. Hartschuh, A. Tip-Enhanced Near-Field Optical Microscopy. *Angew. Chem., Int. Ed.* **2008**, *120*, 8178–8191.
25. Tsen, A. W.; Donev, L. A. K.; Kurt, H.; Herman, L. H.; Park, J. Imaging the Electrical Conductance of Individual Carbon Nanotubes with Photothermal Current Microscopy. *Nat. Nanotechnol.* **2008**, *4*, 108–113.
26. Jorio, A.; Dresselhaus, G.; Dresselhaus, M. S. *Carbon Nanotubes: Advanced Topics in the Synthesis, Structure, Properties and Applications*; Springer Verlag: Berlin, 2008.
27. Knoch, J.; Appenzeller, J. *Carbon Nanotube Field-Effect Transistors—The Importance of Being Small*. Springer Verlag: Berlin, 2006.
28. Maciel, I. O.; Anderson, N.; Pimenta, M. A.; Hartschuh, A.; Qian, H.; Terrones, M.; Terrones, H.; Campos, D. J.; Rao, A. M.; Novotny, L. Electron and Phonon Renormalization near Charged Defects in Carbon Nanotubes. *Nat. Mater.* **2008**, *7*, 878–883.
29. Georgi, C.; Hartschuh, A. Tip-Enhanced Raman Spectroscopic Imaging of Localized Defects in Carbon Nanotubes. *Appl. Phys. Lett.* **2010**, *97*, 143117.
30. Coffey, D. C.; Reid, O. G.; Rodovsky, D. B.; Bartholomew, G. P.; Ginger, D. S. Mapping Local Photocurrents in Polymer/Fullerene Solar Cells with Photoconductive Atomic Force Microscopy. *Nano Lett.* **2007**, *7*, 738–744.
31. Alexe, M.; Hesse, D. Tip-Enhanced Photovoltaic Effects in Bismuth Ferrite. *Nat. Commun.* **2011**, *2*, 256–260.
32. Freitag, M.; Radosavljevic, M.; Zhou, Y.; Johnsona, A. T.; Smith, W. F. Controlled Creation of a Carbon Nanotube Diode by a Scanned Gate. *Appl. Phys. Lett.* **2001**, *79*, 3326–3328.